LAWRENCE
LIVERMORE
NATIONAL
LABORATORY

LLNL-JRNL-698417

Electromagnetic effects on dynamics of high-beta filamentary structures

W. Lee, M. V. Umansky, J. R. Angus, S. Krasheninnikov

July 22, 2016

Physics of Plasmas

Disclaimer

This document was prepared as an account of work sponsored by an agency of the United States government. Neither the United States government nor Lawrence Livermore National Security, LLC, nor any of their employees makes any warranty, expressed or implied, or assumes any legal liability or responsibility for the accuracy, completeness, or usefulness of any information, apparatus, product, or process disclosed, or represents that its use would not infringe privately owned rights. Reference herein to any specific commercial product, process, or service by trade name, trademark, manufacturer, or otherwise does not necessarily constitute or imply its endorsement, recommendation, or favoring by the United States government or Lawrence Livermore National Security, LLC. The views and opinions of authors expressed herein do not necessarily state or reflect those of the United States government or Lawrence Livermore National Security, LLC, and shall not be used for advertising or product endorsement purposes.

LLNL-JRNL-698417

Electromagnetic effects on dynamics of high-beta filamentary structures

Wonjae Lee,[1] Maxim V. Umansky,[2] Justin R. Angus,[3] and Sergei I. Krasheninnikov[1, a)]
[1)] *University of California, San Diego, 9500 Gilman Drive, La Jolla, California 92093, USA*
[2)] *Lawrence Livermore National Laboratory, 7000 East Avenue, Livermore, California 94550, USA*
[3)] *Naval Research Laboratory, 4555 Overlook Avenue, Washington, DC 20375, USA*

(Dated: 17 September 2014)

The impacts of the electromagnetic effects on blob dynamics are considered. Electromagnetic BOUT++ simulations on seeded high-beta blobs demonstrate that inhomogeneity of magnetic curvature or plasma pressure along the filament leads to bending of the blob filaments and the magnetic field lines due to increased propagation time of plasma current (Alfvén time). The bending motion can enhance heat exchange between the plasma facing materials and the inner SOL region. The effects of sheath boundary conditions on the part of the blob away from the boundary are also diminished by the increased Alfvén time. Using linear analysis and the BOUT++ simulation, it is found that electromagnetic effects in high temperature and high density plasmas reduce the growth rate of resistive drift wave turbulence when resistivity drops below some certain value. In the course of blobs motion in the SOL its temperature is reduced, which leads to enhancement of resistive effects, so the blob can switch from electromagnetic to electrostatic regime, where resistive drift wave turbulence become important.

PACS numbers: 52.25.Fi, 52.35.Kt, 52.35.Ra, 52.40.Kh

I. INTRODUCTION

Plasma blobs (filamentary structures extended along the magnetic field lines) are meso-scale turbulent structures usually observed in the scrape-off layer (SOL) of magnetic confinement devices. They are characterized by it's convective behavior propagating with velocity V_b reaching several percent of sound speed. Typical blob size is $\sim 1-3$ cm and plasma density in the blob is significantly higher than that of ambient plasma. In tokamaks blobs appear on the outer side of the torus.

Blobs, which are inherent part of edge plasma turbulence and transport, controlling plasma-wall interactions, have been extensively studied in last decade. Comprehensive reviews on blobs can be found in Ref. 1 and Ref. 2. The basic theory of blob physics was introduced in Ref. 3. The charge separation caused by effective gravity (caused by curvature and grad(B) effects) results in a radial $E \times B$ convection of plasma. The blob dynamics is sensitive to the interplay between cross field polarization current and the current along the field lines which is the subject of various closures[1]. Recent study of the impact of plasma instabilities on blob dynamics show that the coherency of the blob can be substantially limited by the onset of the resistive drift wave instability resulting in blobs dispersion[4]. However only electrostatic limit was considered in Ref. 4.

The impact of particle and heat transported by blobs on plasma-facing components become more significant as the pressure of plasma in the blobs increases. These large-pressure blobs can be formed by the edge localized mode (ELM) crashes or by turbulent activities in the SOL of large confinement machines. In the case of the increased plasma beta ($\tilde{\beta} \equiv \beta M_{\rm i}/m_{\rm e} > 1$, $\beta = 8\pi nT/B^2$) the electromagnetic effects become important. Theoretical work on such electromagnetic blob regimes and their effects on the blob dynamics can be found in Refs. 1, 5–8. Although some electromagnetic turbulent simulations[9,10] on tokamak SOL also have been performed, there has been virtually no attention to the electromagnetic effects on high-β blob dynamics.

In this paper, we present the result of our studies of the electromagnetic effects on the seeded high-β blob dynamics and stability with BOUT++ framework[11,12]. In addition, we supplement our numerical simulations with analytic estimates of blob stability in electromagnetic regime.

The paper is organized as follows: In Section II we present equations we use to describe blob dynamics and stability in electromagnetic regime; In Section III we consider an impact of electromagnetic effects on macroscopic blob dynamics; In Section IV we analyze influence of electromagnetic effects on resistive drift wave instability of blob's plasma; In Section V we discuss our results and in Section VI we summaries our main conclusions.

II. GOVERNING EQUATIONS, INITIAL AND BOUNDARY CONDITIONS

A. Governing equations

We consider blob's plasma dynamics using fluid approximation and a three-dimensional Cartesian geome-

[a)] skrash@mae.ucsd.edu

try with z-coordinate aligned to magnetic field, $\mathbf{B}$, and x-, y-coordinate corresponds to the radial and effective poloidal direction respectively. Essential physics of blob dynamics can be simplified to isothermal electron dynamics and ignoring ion parallel motion and ion temperature effects[4].

Using the Boussinesq approximation, gives reasonably accurate results[13], we have the following set of equations[11,12]

$$\frac{e\rho_{\rm s}^2}{T_{\rm e}} n \frac{\rm d}{\rm dt}\left(\nabla_\perp^2 \phi\right) = \frac{1}{e}\nabla_\parallel J_\parallel - \frac{g}{\Omega_{\rm i}}\frac{\partial n}{\partial y}, \tag{1}$$

$$\frac{{\rm d}n}{{\rm dt}} = \frac{1}{e}\nabla_\parallel J_\parallel - \frac{g}{\Omega_{\rm i}}\frac{\partial n}{\partial y}, \tag{2}$$

$$\frac{{\rm d}A_{j\parallel}}{{\rm dt}} = \frac{e}{m_{\rm e}}\frac{\partial \phi}{\partial z} - \frac{T_{\rm e}}{m_{\rm e}}\nabla_\parallel \ln n + \frac{e}{\sigma_\parallel m_{\rm e}} J_\parallel, \tag{3}$$

where n is the plasma density, ϕ is the electrostatic potential, $T_{\rm e}$, $m_{\rm e}$ and $-e$ are the electron temperature, mass and charge respectively, $\rho_{\rm s} = c_{\rm s}/\Omega_{\rm i}$ is gyro-Bohm radius, $c_{\rm s} = (T_{\rm e}/M_{\rm i})^{1/2}$ is ion sound speed, $\Omega_{\rm i}$ is the ion gyro-frequency, $M_{\rm i}$ is ion mass, $g = 2c_{\rm s}^2/R$ is the effective gravitational acceleration representing polarization drive due to the magnetic curvature and grad(B) effects, R is the tokamak major radius, $\sigma_\parallel \propto T_{\rm e}^{3/2}$ is the plasma electric conductivity along the magnetic field, the derivative operators are defined as ${\rm d}/({\rm dt}) = \partial/(\partial t) + (c/B)\hat{\rm b}_0 \times \nabla\phi\cdot\nabla$ and $\nabla_\parallel = \partial/(\partial z) + (\nabla A_\parallel/B_0)\times\hat{\rm b}_0\cdot\nabla$, and where $\hat{\rm b}_0$ is the unit vector along the unperturbed magnetic field, $A_{j\parallel}$ is defined as summation of the parallel component of vector potential and an electron inertia term,

$$A_{j\parallel} \equiv -\frac{eA_\parallel}{m_{\rm e}c} - \frac{J_\parallel}{ne}, \tag{4}$$

where c is the speed of light. The parallel vector potential $A_\parallel$ is calculated by the inversion of following relation,

$$J_\parallel = -\frac{c}{4\pi}\nabla_\perp^2 A_\parallel. \tag{5}$$

Equations (1-5) provide three coupled equations for ϕ, n and $A_{j\parallel}$ governing the electromagnetic blob dynamics

B. Initial and boundary conditions

Solving the given system of Eqs. (1-5), requires boundary and initial conditions of all variables. Following Refs. 4 and 14 we consider initial plasma density as a homogeneous background and with a bump on it, $n = n_0 + \tilde{n}(\mathbf{x})$, with $\tilde{n}(\mathbf{r}) = \tilde{n}_{\rm b}\exp\left[-((x-x_0)^2 + (y-y_0)^2)/\delta^2\right]$, where (x_0, y_0) is the initial location of blob's center of mass in transverse plane and δ is a characteristic blob radius. We take zero of all other variables at the beginning of the simulations.

The conditions of electric potential, density and current density at the domain boundary along the magnetic field lines play important roles in blob dynamics. We apply Neumann conditions at the upper (+) and the lower (−) boundaries in z-directions for density, $\partial n/(\partial z)|_\pm = 0$. The sheath limited boundary condition for electric potential can be one possible choice because parallel magnetic fields end at a material surface in an open magnetic configuration such as the SOL. Given the condition we have current limit through the sheath boundary in z-direction,

$$J_{{\rm sh}\pm} = \pm\frac{c_{\rm s}e^2}{T_{\rm e}} n_\pm \phi_\pm, \tag{6}$$

where $n_\pm$ and $\phi_\pm$ are the density and the electric potential at the upper and the lower sheath boundaries, respectively. Assuming field line bending is small at the sheath boundary region, the current density near the sheath region is represented as

$$J_{\parallel\pm} = \sigma_\parallel \frac{\partial\phi}{\partial z}\Big|_\pm - \frac{\sigma_\parallel}{c}\frac{\partial A_\parallel}{\partial t}\Big|_\pm. \tag{7}$$

Matching current density of Eq. (6) with that of Eq. (7), we determine the sheath limited boundary condition for electric potential. We use constant gradient conditions at the sheath boundaries for parallel current, i.e. $\partial j_\parallel/(\partial z)|_{{\rm sh}\pm} = \partial J_\parallel/(\partial z)|_\pm$ assuming continuous polarization.

It is worthwhile noting here that the boundary conditions of high-β filaments may not have the sheath limited condition. In other words, the physical locations of the longitudinal terminal points of the filaments can be actually inside the separatrix not on the material surfaces[2]. In this case determining exact boundary conditions along the field line is difficult because the conditions are to be coupled to the plasma parameters near the interface between the core and edge region.

Therefore, in addition to the sheath limited boundary condition that describes the parallel interface between a filament and material surface, we can also consider a simple boundary condition that disconnects the filament from the surface. This free boundary condition is given as Neumann condition on electric potential and density, $\partial\phi/(\partial z)|_\pm = \partial n/(\partial z)|_\pm = 0$, and a Dirichlet boundary condition on the parallel current density, $J_\parallel|_\pm = 0$. The situation where $J_\parallel|_\pm$ is zero corresponds roughly to the case where the filament is located near the X-point of magnetic topology in magnetic confinement devices. Increasing effective resistivity in the X-point region hinders parallel currents and the filament regime is electrically disconnected from the sheath boundary and approaches the resistive ballooning regime[2,6].

III. ELECTROMAGNETIC EFFECTS ON BLOB PROPAGATION

A. Electromagnetic effects and sheath boundary condition

As stated in section I, blob dynamics is determined by the dipole potential resulted from the balance between

perpendicular polarizing current and parallel current. Therefore, boundary conditions for the parallel current become an important factor in blob dynamics. In electrostatic approximations, boundary conditions (e.g. sheath limited conditions) have immediate effects on blob dynamics throughout the whole filamentary length, whereas in electromagnetic calculations the boundary effects are minimized by retarded Alfvén speed at high-β plasmas.

For the purpose of comparing boundary effects on electromagnetic and electrostatic high-β blobs, we perform 3D simulation using BOUT++ code[11,12]. Considering an ITER relevant machine, the radius of curvature and the connection length are set to $R \sim 6$ m and $L \sim 100$ m respectively. As an initial condition we seed a blob with a Gaussian function $n/n_0 = 1 + 2\exp[-(x^2 + y^2)/\delta^2]$. The plasma is considered to have high-β as $\tilde{\beta} \sim 3$ for $T_\mathrm{e} = 200$ eV, $n_0 = 1 \times 10^{14}$ cm^{-3} and $B = 5.3$ T. Note that these plasma parameters are somewhat higher than that of predictions made by two dimensional modeling on core-edge plasma for the ITER machine[15]. The parameters for the high-β filament corresponds to a plasma with a collisional regime satisfying $\lambda_\mathrm{e}/L \sim 0.02 \ll 1$. The cross sectional blob size is set to the characteristic size $\delta = \delta_* \equiv \rho_\mathrm{s}(gL^2/(4c_\mathrm{s}^2\rho_\mathrm{s}))^{1/5}$ as in Refs. 1 and 4.

The results from electromagnetic and electrostatic calculations for the sheath boundary condition using the high-β parameters with blob size $\delta/\delta_* = 1$ are shown in Fig. 1. The 2D density contours are obtained by taking average along the field line. Notice that the averaged density contours from the electromagnetic simulation (top) develop "mushroom" shape and propagate in radial direction with faster speed while electrostatic simulation (bottom) shows virtually no "mushrooming".

The reason for this discrepancy is that the parallel current development mechanism is different in the two calculations. Due to immediate formation of the Ohmic current along the magnetic field lines, the electrostatic calculation causes polarized charges to be quickly flow to sheath boundary. But in electromagnetic case, parallel current propagates toward the sheath with Alfvén speed. As a result, for the case where Alfv'en time, $\tau_A = L/v_A$, is larger than characteristic blob propagation time, $\tau_b = \delta/V_b$, electromagnetic simulations give higher polarization potential (see Fig. 2) and, consequently, higer speed, which finally causing "mushrooming". We also note that the slow development of parallel current may lead to the bending of filament. Further explanation on this electromagnetic bowing of filamentary structure will be given in following subsection.

Estimating τ_b for structurally stable blob size[1], $\delta = \delta_*$, we find $\tau_A/\tau_b = \beta^{1/2}(L^4/\rho_\mathrm{s}^2/R^2)^{1/5}$. For the parameters we used for our simulations $\tau_A/\tau_b \sim 4$.

B. Electromagnetic effects and inhomogeneous polarization

In previous sub-Section we consider the case of homogeneous initial blob density along the magnetic field lines and constant g. However, in practice both blob plasma density and g can vary along the magnetic field lines (e.g. recall that g has different sign on outer and inner torus sides in a tokamak). This will cause non-homogeneous polarization of blob resulting in variation of velocities of different parts of blob and blobs shape bending along the magnetic field lines. We also notice that non-uniform blob plasma density distribution along the field line can cause blob spinning[4].

We performed three dimensional numerical simulations of high-β seeded blobs in a varying curvature for the electromagnetic and the electrostatic calculations. For the demonstration of filament bending, we consider a simple curvature variation in a form $\kappa_\mathrm{x} \sim -\sin^2(\pi z/(2L))/R$ in the Cartesian computational frame. Under this condition, the value of the curvature has zero (neutral) at the end points and the maximum (unfavorable) at the midpoint of the filament. The free boundary conditions were used in the z-direction. The Neumann and the periodic boundary conditions were applied for x and y-direction respectively. A cylindrical blob with cross sectional size with $\delta \sim 0.5$ cm is seeded at $t = 0$. And other blob parameters are same as those of the sheath limited blob simulation.

The sequence of normalized blob density from the electromagnetic and the electrostatic simulation is shown in Fig. 3. The comparison between electromagnetic and electrostatic simulation demonstrates how the filamentary structure is bent by electromagnetic effects. The electromagnetic simulation shows a non-uniform motion along the filament: a strong radial movement in the most unfavorable curvature location and a rather delayed radial motion near the neutral curvature region. Meanwhile for electrostatics, the radial motion shows uniform distribution along the filament despite the inhomogeneous curvature field.

The reason for such discrepancy between the electromagnetic and electrostatic simulation is large ratio $\tau_A/\tau_b \sim 4$, which slows down parallel current propagation which could equilibrate potential along the magnetic field lines. In Fig. 4 one can see the evolution of maximum potential difference distribution along the field line for the two simulations. The non-uniform potential distribution in the electromagnetic filament slowly becoming uniform, while the electrostatic calculation is macroscopically uniform from the beginning. It is also interesting to see that the electromagnetic simulation did not produce instability at the time when the electrostatic approximation showed the resistive drift wave instability sometime around $t \sim 5$ μs. More details on this microscopic effects will be discussed in Sec. IV.

The maximum difference of convection speed can be estimated by normalization of the vorticity equation with

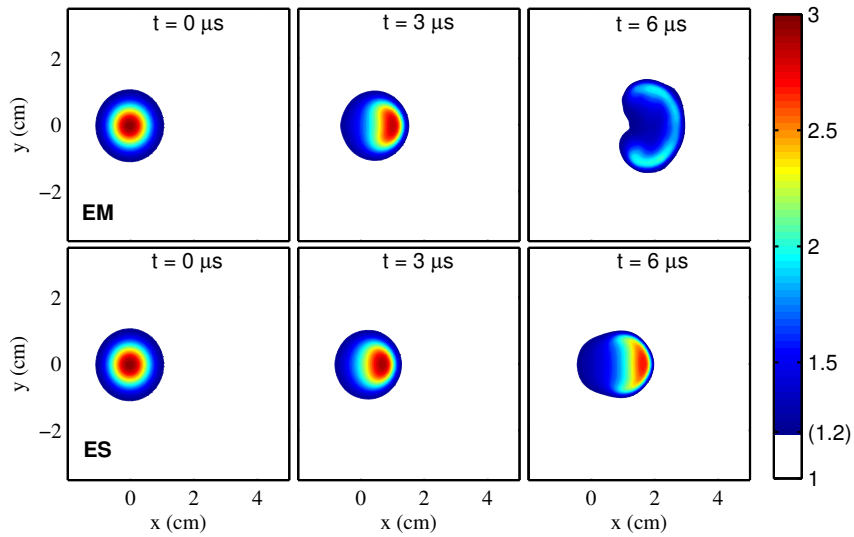

FIG. 1. Comparison of the sheath limited high-β blob evolution from electromagnetic (top) and electrostatic calculation (bottom) for balanced size blob ($\delta/\delta_* = 1$). The 2D contours are the averaged value along the field line.

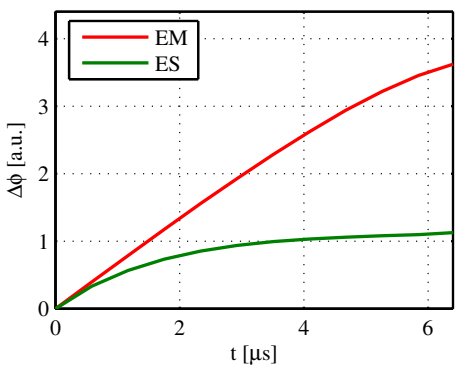

FIG. 2. Comparison of the dipole potential strength in the sheath limited high-β blobs for electromagnetic (red) and electrostatic calculation (green).

Alfvén time. From the vorticity equation, Eq. (1), the maximum difference of $E \times B$ velocity between center and boundary region of Alfvén wave emitting blob is estimated as

$$\Delta v_x(t) \simeq \beta^{1/2} \frac{L}{R} c_s G(\kappa, n) \frac{t}{\tau_A} + F(J_\parallel(t)), \tag{8}$$

where $G(\kappa, n) = 1 - \kappa_{z=L} n_{z=L} / (\kappa_{z=L/2} n_{z=L/2})$ is a geometrical weighting factor with order of ~ 1 considering the ratio of the most unfavorable ($z = L/2$) and most favorable ($z = L$) curvature and the ratio of inhomogeneous filament density along the field line. F is a function of parallel current that makes the velocity difference become small after $t \sim \tau_A$. Integrating the velocity difference, we get an expression for the filament bending

$$\Delta x_{\text{bending}} \lesssim \int_0^{\tau_A} \Delta v_x(t) \mathrm{d}t \sim \frac{1}{16} \beta \frac{L^2}{R} G(\kappa, n). \tag{9}$$

Similar scaling of line bending for high plasma pressure filament was also obtained in Ref. 5.

The Alfvén wave emitting electromagnetic filament will also involve the bending of magnetic field as well as the bending of plasma filament. The inhomogeneous three dimensional blob simulation cause the development of current dipole for the both electromagnetic and electrostatic simulations. (See Fig. 5). Note that this kind of current dipole is also formed in the filaments with sheath boundary condition. The magnetic field line bending caused by the current dipole is estimated as

$$\Delta x_{\text{mag}} \sim \int_0^{L/2} \left| \frac{B_x}{B} \right| \mathrm{d}z \lesssim \frac{1}{16} \beta \frac{L^2}{R} G(\kappa, n). \tag{10}$$

The field line bending Eq. (10) follows same form as the plasma bending Eq. (9). This suggests that the magnetic field lines will be "frozen-in" to the high-β filament. Fig. 6 shows the "frozen-in" field lines with density contour slices in time. In the electromagnetic calculation (top row of Fig. 6), the magnetic field line (red curve online) threading the center of blob shows synchronized motion with peak density at $t = 2\ \mu s$. In the electrostatic simulation, however, the magnetic field lines are recomposed from the Ohmic current and they do not show the frozen-in motion.

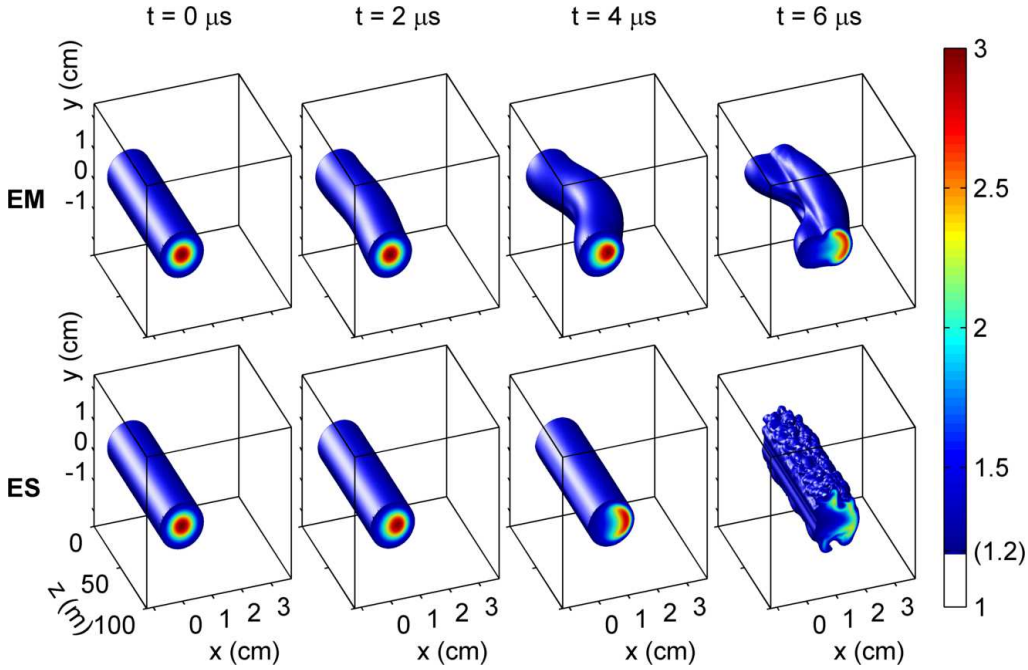

FIG. 3. Evolution of density (n/n_0) for the high-β filament in the varying curvature along the field line from electromagnetic (top) and electrostatic (bottom) calculations.

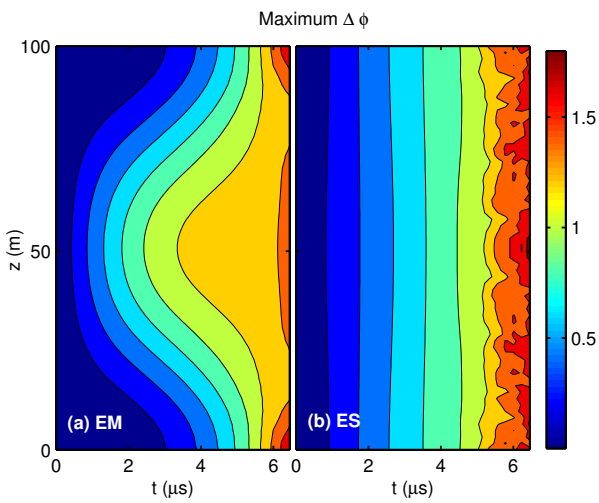

FIG. 4. Comparison of the dipole potential evolution for (a) electromagnetic and (b) electrostatic calculation on high-β filament submerged in the inhomogeneous curvature field. The maximum value of potential difference is calculated over the drift (x,y) plane in location z at time t.

IV. ELECTROMAGNETIC EFFECTS ON BLOB STABILITY

So far we discussed on the macroscopic effects on blob dynamics. However, as we have seen in Figs. 3-6, there are also different behaviors in the microscopic activities between electrostatic and electromagnetic calculations. The resistive drift wave instability (RDWI) from the electrostatic approximation is modified by the electromagnetic and electron inertia perturbations. When the resistive effect becomes small due to increased electron temperature, the electrostatic approximation is not enough to describe the system and the wave instability should be described by electromagnetic terms. In the high temperature plasmas, the wave instability can be either modified by electromagnetic drift-Alfvén wave with reduced growth rate or enhanced by the electron inertia instability.

To evaluate the onset of plasma turbulence of filamentary structures, we perform a local linear stability analysis. We consider exponentially decaying density $\partial \ln n/(\partial x) = -1/\delta$. This decaying density profile can represent the seeded blob with Gaussian density profile at the local point half radius away ($|x - x_0| \sim \delta/2$) from the center of blob. The normal mode perturbation of density, electric potential and parallel vector potential are assumed to have the form $\exp(i\mathbf{k}\cdot\mathbf{r} - i\omega t)$, where $\mathbf{k}$ is wave number vector. Carrying out an analysis similar to that of Ref. 4, we get the following dispersion equation

$$\omega^2 + \omega_{\rm g}^2 - \omega\frac{g\chi}{c_{\rm s}} = -i\omega_{\parallel}^{\rm EM}\left(\omega - \frac{\omega_*}{1+\chi^2}\right), \qquad (11)$$

where

$$\omega_{\parallel}^{\rm EM} = i\omega_A^2\frac{(1+\chi^2)}{\left(\omega - \omega_* + \omega\frac{k_\perp^2 c^2}{\omega_{\rm pe}^2} + i\frac{k_\perp^2 c^2}{4\pi\sigma_\parallel}\right)}, \qquad (12)$$

and $\omega_{\rm g} = \sqrt{g/\delta}$ is flute mode growth rate, $\omega_* = k_y c_{\rm s}\rho_{\rm s}/\delta$ is a drift frequency, $\omega_A = k_z v_A$ is the Alfvén frequency

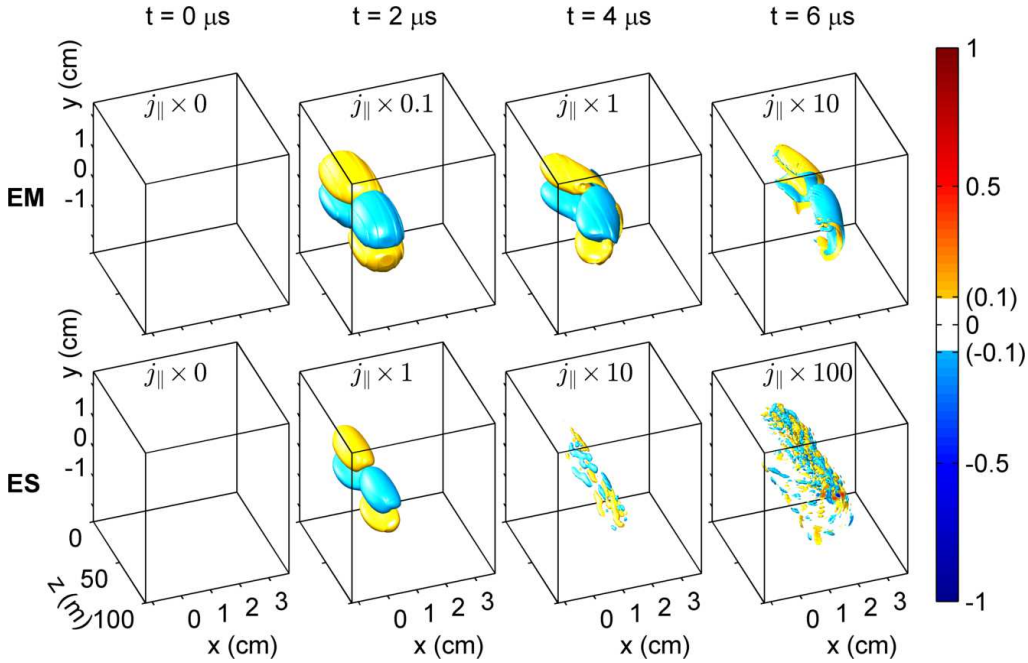

FIG. 5. Evolution of parallel current ($j_\parallel$) for the high-β filament in the varying curvature along the field line from electromagnetic (top) and electrostatic (bottom) calculations .

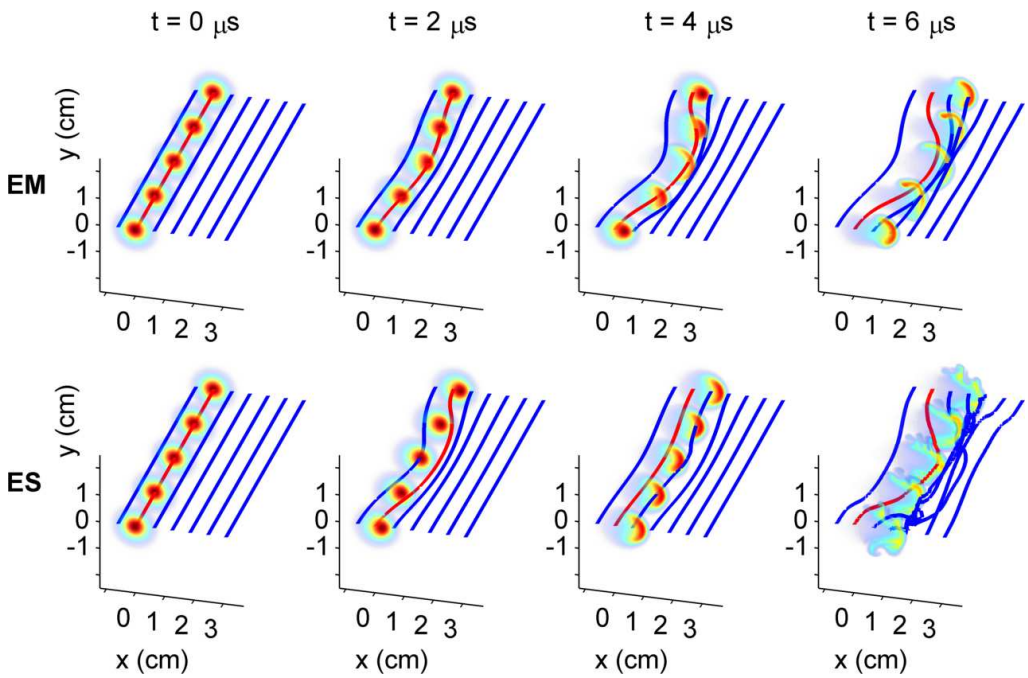

FIG. 6. Magnetic field line bending for the high-β filament in the varying curvature along the field line from electromagnetic calculation (top). For the electrostatic calculation (bottom), the magnetic field are calculated by inversion of electrostatic current. Blue and red lines are the total magnetic field line. The red curve represents the magnetic field line with initial location of filament.

and $\chi = k_y \rho_s$ is a normalized perpendicular wave number with $k_x \rho_s \ll 1$ approximation.

When $\omega_g^2 \gg \omega_A^2$ is satisfied, the wave instability is dominated by flute mode, $\omega \sim i\omega_g$. This radial motion driven by the gravitational (curvature) force will significantly modify the initial approximation of the local density profile, $n \sim \exp(-x/\delta)$. Therefore, we simplify the dispersion relation neglecting gravity (curvature) effects by con-

sidering high parallel wave number case $k_z \gg \omega_g/v_A$.

Within a drift frequency ordering, it is useful to normalize the previous dispersion relation with a frequency scale free from wave number. If we consider a normalizing parameter $\hat{\omega}_* \equiv c_s/\delta = \omega_*/\chi$, we get the representation of perpendicular and parallel wave number by χ and ω_A respectively. Then, the normalized dispersion relation is

$$\Omega^2 \left[\Omega - \chi + \frac{\Omega\chi^2}{\tilde{\beta}} + i\Omega_R\chi^2\right] = \Omega_A^2 \left[\Omega(1+\chi^2) - \chi\right], \tag{13}$$

where $\Omega \equiv \omega/\hat{\omega}_*$ is a normalized wave frequency, $\Omega_R = c^2/(4\pi\sigma_\parallel \rho_s^2 \hat{\omega}_*)$ is a normalized collision frequency and $\Omega_A = \omega_A/\hat{\omega}_*$ is a normalized Alfvén frequency.

In the LHS bracket of Eq. (13), the first two terms correspond to the electromagnetic responses; the first term originated from the time derivative of parallel vector potential, $\partial A_\parallel/(\partial t)$ and the second term correlate with the field line bending term, $\nabla A_\parallel/B_0 \times \hat{\mathrm{b}}_0 \cdot \nabla \ln n$. On the other hand the third and fourth term correspond to two kinds of dissipation terms; the electron inertia term, $\tilde{\beta}^{-1}\chi^2\Omega$, describes the "unfrozenness" of magnetic field on a scale length of the order of collisionless skin depth and the fourth term, $i\Omega_R\chi^2$, explains the plasma resistivity.

Initially we begin the stability analysis of Eq. (13) by considering electrostatic limit as a reference. If the resistivity term, $i\Omega_R\chi^2$, dominates other electromagnetic and electron inertial terms in the drift wave frequency range, such that $\Omega_R \sim \delta \cdot B^2/T_e^3 \gg 1 + \tilde{\beta}^{-1}$ is satisfied, then we get the following electrostatic dispersion relation similar to the equation found in Ref. 4,

$$\Omega^2\Omega_R\chi^2 + i\Omega_A^2\left[\Omega(1+\chi^2) - \chi\right] = 0. \tag{14}$$

In this case, this wave dispersion relation describes drift wave as $\Omega^2(\Omega_A^2 \to \infty) = (\chi/(1+\chi^2))^2$. The growth rate of the resistive drift wave is found to be

$$\frac{\gamma}{\hat{\omega}_*} = \left\{\sqrt{\frac{\xi^4}{4} + \left(\frac{\chi}{1+\chi^2}\right)^2 \xi^2} + \frac{\xi^2}{2}\right\}^{1/2} - \xi, \tag{15}$$

where $\xi = (1+\chi^2)\Omega_A^2/(2\chi^2\Omega_R)$. The growth rate shows asymptotic behaviours such $\gamma/\hat{\omega}_*(\xi \to 0) = \sqrt{\xi/2}$ and $\gamma/\hat{\omega}_*(\xi \to \infty) = 1/(8\xi)$. The maximum growth rate of the electrostatic resistive drift wave instability is found to be $\gamma_{\max}/\hat{\omega}_* \sim 0.15$ without a dependency on Ω_R for $\xi \simeq 0.24$ with $\chi = 1$.

We next consider following an ideal electromagnetic dispersion equation by neglecting dissipation terms $(\Omega\chi^2\tilde{\beta}^{-1} + i\Omega_R\chi^2)$ from Eq. (13). This condition can be achieved from high beta ($\tilde{\beta}^{-1} \to 0$) and high temperature ($\Omega_R \to 0$) plasma. For $\chi \sim 1$, $\Omega_A^2 \gg 1$ limit, we get a drift wave with frequency, $\Omega = \chi/(1+\chi^2) \leq 1 \ll \Omega_A$, and outward emitting dispersive Alfvén waves, $\Omega^2 = \Omega_A^2(1+\chi^2)$. For $\Omega_A^2 \ll 1$, we get a drift wave

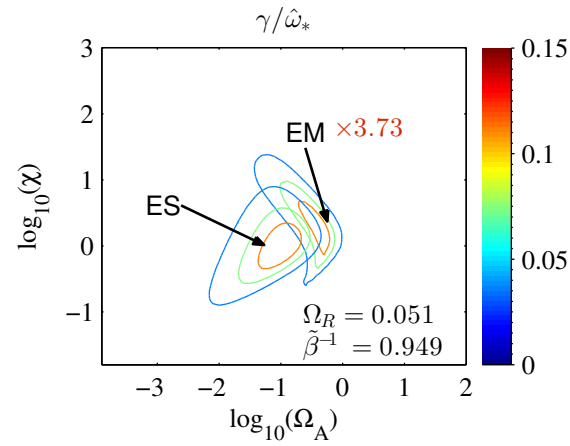

FIG. 7. Normalized growth rate $\gamma/\hat{\omega}_*$ as function of Ω_A and χ for two different models: electromagnetic (EM) and electrostatic (ES) calculation. Note that the EM growth rate represents drift-Alfvén wave and is multiplied by 3.73 for clarity. The parameters Ω_R and $\tilde{\beta}^{-1}$ correspond to a high beta plasma with $T_e = 200$ eV, $n_0 = 1 \times 10^{14}$ cm^{-3}.

($\Omega = \chi$) and two Alfvén waves ($\Omega^2 = \Omega_A^2$). The dispersion equation has three distinctive real roots for $\chi > 1$, $\Omega_A > 0$. Therefore, all three waves are stable in the ideal electromagnetic case. However, a small resistive correction ($\Omega_R < 1$) can make the drift wave unstable. Neglecting the electron inertia term, we find that: for $\Omega_A^2 \gg 1$, the growth rate of the resistive drift wave is estimated as $\gamma/\hat{\omega}_*(\chi \sim 1) \sim \Omega_R\chi^4/(\Omega_A^2(1+\chi^2)^3)$ and $\gamma/\hat{\omega}_*(\chi \gg 1) \sim \Omega_R/(\Omega_A\chi)^2$; for $\Omega_A^2 \ll 1$, the growth rate is approximately $\gamma/\hat{\omega}_*(\chi \gg 1) \sim (\Omega_A^2\chi\Omega_R/(1+\Omega_R^2\chi^2))^{1/2}$. Thusly in contrast to the electrostatic case where $\gamma_{\max}/\hat{\omega}_* \sim O(1)$ and is independent of Ω_R, the electromagnetic case exhibits a strong reduction in the growth rate: $\gamma_{\max}/\hat{\omega}_* \leq \Omega_R \ll 1$.

Figure 7 shows the contour lines of normalized growth rate of drift wave instability from numerical calculation of the electromagnetic equation (13) and the electrostatic dispersion equation (14) for plasma parameters with $T_e = 200$ eV and $n_0 = 1 \times 10^{14}$ cm^{-3}. The maximum normalized growth rate of this drift-Alfvén wave is about 3.73 times smaller than that of the electrostatic resistive drift wave instability with maximum value 0.15. The value of the contour lines from the electromagnetic calculations are multiplied by a factor 3.73 for better visibility. This reduction of instability is also observed in fluid simulations using BOUT++ (See Figure 8).

The interaction between the magnetic field lines and the high-β plasma plays a role in the suppression of drift wave turbulence. When the density of filaments have sufficiently high value of β, the filament carries "frozen-in" magnetic field lines. When the resistive drift waves grow, the perturbed parallel currents due to the drift waves will induce perpendicular magnetic fields resulting in net helical field lines in low-β plasma. Unlike the electrostatic case, however, the perturbed magnetic field

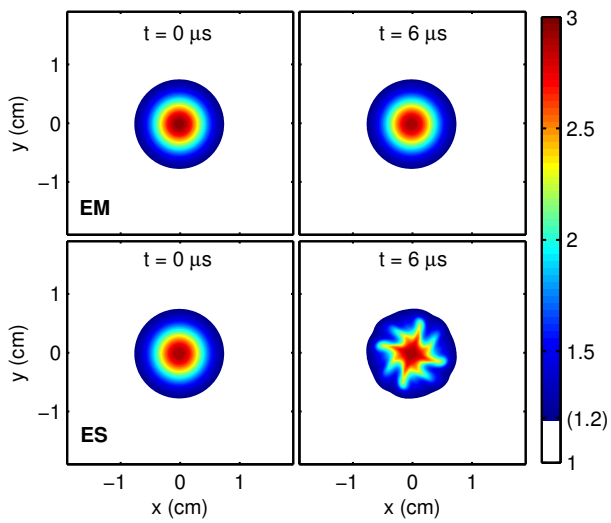

FIG. 8. Blob density contours of high-beta plasma from EM (top) and ES (bottom) models. The electrostatic model shows resistive drift wave. The effective gravity force is suppressed for simplicity

should move with plasma elements in electromagnetic high-β case. Because the free energy of instability should modify the whole system including magnetic fields and plasmas, the electromagnetic effects makes the instability to grow much slower than the electrostatic case. Moreover distorting motions of plasma element will cause local bending magnetic field and this bent magnetic field exert restoring force on the plasma perturbation.

Comparing the contour lines in Fig. 7 obtained with the electromagnetic and electrostatic models, we can see that the most unstable normalized perpendicular and parallel wave numbers are higher in the case of electromagnetic model. The dependencies of most unstable parallel wave numbers, which correspond to maximum growth rates, and resistivity are found to be $(\Omega_A)_{\gamma_{\max}} \sim \max[\Omega_R, \tilde{\beta}^{-1}]^{1/2}$. For $\tilde{\beta}^{-1} > 1$, the most unstable perpendicular wave number is $(\chi)_{\gamma_{\max}} \sim 1$, and for the conditions $\tilde{\beta}^{-1} < 1$ and $\Omega_R < 1$, the empirical relation is found to be $(\chi)_{\gamma_{\max}} \sim \Omega_R^{-1/2}$.

We note that in our analysis we assume zero ion temperature. In practice, ion temperature in edge plasma is often larger than electron one. Therefore, finite Larmor radius effect can become important for $\tilde{\beta}^{-1} < 1$ and $\Omega_R < 1$ where perpendicular wave length of the most unstable mode is relatively small.

Meanwhile, the electron inertial term can also make the dispersion relation have imaginary roots. The condition which increases the electron inertial effect will be achieved with high $T_{\rm e}$ but relatively low-β so that both $\Omega_R \chi^2 < \Omega$ and $\tilde{\beta}^{-1}\chi^2 \gg 1$ conditions are satisfied. In this case, the maximum growth rate of electron inertial instability is found to be $\gamma/\hat{\omega}_* \sim 0.3$ at $\Omega_A^2 \tilde{\beta} \sim 0.5$ with

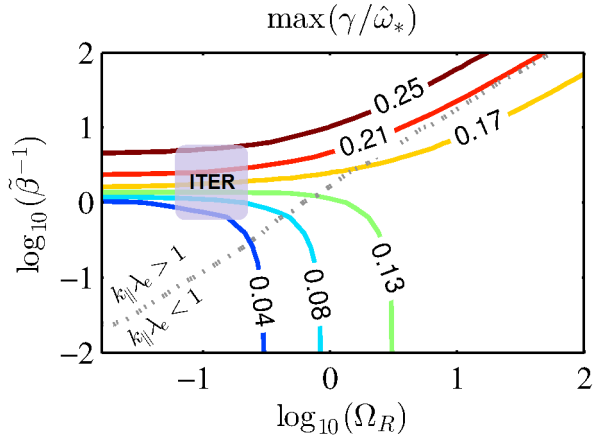

FIG. 9. Contour lines of normalized maximum growth rate as function of resistivity and $\tilde{\beta}^{-1}$ and a line (dotted) $k_\parallel \lambda_{\rm e} = 1$ with respect to $\Omega_A(\gamma_{\max})$

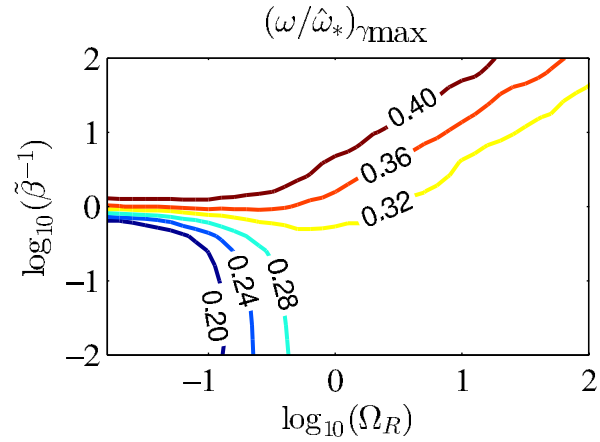

FIG. 10. Contour lines of normalized real frequency of the corresponding maximum growth rate (Fig.9) as function of resistivity and $\tilde{\beta}^{-1}$.

$\chi \sim 1$.

Figure 9 shows the normalized maximum growth rate as a function of resistivity and plasma beta. The figure reveals three distinct instability regimes: Electromagnetic drift-Alfvénic suppression regime, electron inertial instability regime and electrostatic resistive drift wave instability regime. For high temperature ($\Omega_R \ll 1$) and high pressure ($\tilde{\beta} \gg 1$) regime, electromagnetic effects reduce the growth rate of the resistive drift wave instability. However, the electron inertial dissipation increases the growth rate of the electron inertial instability for relatively low pressure regime ($\log_{10} \tilde{\beta}^{-1} > 0$). In the high temperature regime, the density determines whether the drift wave instability become suppressed or the electron inertial instability becomes unstable. For the electromagnetic regime $T_{\rm e} > (B^2\delta)^{(1/3)}$, the electron inertial instability becomes important if the density is lower than

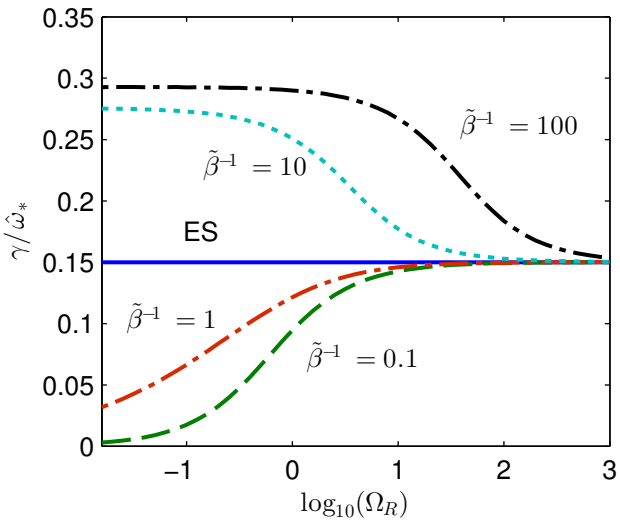

FIG. 11. Maximum normalized growth rate $\gamma/\hat{\omega}_*$ as a function of resistivity parameter Ω_R for electromagnetic blobs of four different values of $\tilde{\beta}^{-1} = 0.1, 1.0, 10, 100$ and electrostatic blob with electron inertia neglected (blue solid line).

certain value,

$$n < n_{\rm crit}[{\rm cm}^{-3}] \equiv 6.75 \times 10^{14} \frac{B[{\rm T}]^2}{T_{\rm e}[{\rm eV}]}. \qquad (16)$$

When electron temperature decreases, we get the electrostatic resistive drift instability regime with the dominate resistive term.

We note that a range of plasma parameters, from the typical SOL plasmas ($T \sim 100$ eV, $n \sim 3 \times 10^{13}$ cm^{-3}) for ITER[15] to some enhanced parameters with density ($n \sim 1 \times 10^{14}$ cm^{-3}) considering the ELM event, presents somewhat marginal regime between the two electromagnetic regimes. This suggests that turbulence produced blobs within the relatively less dense background plasmas are likely to have electron inertial instability while high-density plasmas from the ELM crash or from pellet ablation will be less unstable. However, when the plasma is resistive, $\Omega_R \gg 1 + \tilde{\beta}^{-1}$, both electromagnetic suppression and the electron inertial instability effects become negligible electrostatic and the system becomes electrostatic. See Fig. 11.

There are some limitations on the applicability of the fluid approximation on electromagnetic regimes. First of all, the mean free path along the field line should be shorter than parallel wave length of the most unstable wave to make the fluid equation is valid (See Fig. 9). In terms of stability analysis, this collisionality condition, $k_{\parallel,\gamma_{\rm max}}\lambda_{\rm e} < 1$, sets more severe restriction to the validity of fluid approximation $\lambda_{\rm e}/L \ll 1$. For example, if we use the relation $k_{\parallel,\gamma_{\rm max}}\lambda_{\rm e} = \tilde{\beta}^{-1/2}(\Omega_A)_{\gamma_{\rm max}}/\Omega_R < 1$ with $(\Omega_A)_{\gamma_{\rm max}} \sim \max[\Omega_R, \tilde{\beta}^{-1}]^{1/2}$, then the required density for fluid approximation is $n[{\rm cm}^{-3}] > 3 \times 10^{10} T_{\rm e}[{\rm eV}]^2/\delta[{\rm cm}]$. This relation has second order dependency in electron temperature. Considering high temperature ($T_{\rm e} > 100$ eV), the validity of fluid approximation in the stability analysis is questionable for typical densities in the SOL region.

Moreover, the collisionality condition regarding the ratio of the collision frequency to the wave frequency for the maximum growth rate ($\nu/\omega_{\gamma_{\rm max}} \gg 1$) is also required for the validity of fluid approximation. Because the wave frequency for the maximum growth rate is comparable to the drift frequency, $\omega_{\gamma_{\rm max}} \lesssim \hat{\omega}_*$, the collisionality condition becomes approximately $\nu/\hat{\omega}_* > 1$. This condition also results in similar density requirement as $k_\parallel \lambda_{\rm e} < 1$ condition for the fluid approximation. Consequently we remark that the kinetic approach is needed for more realistic analysis on the dynamics of SOL region and the kinetic effects may modify the stability of plasma away from the estimation made by fluid approximation.

It should be noted that the kinetic effects, resulting in Landau damping, are missing in our fluid approximation. Meanwhile, for the case where drift wave instability is related to the effects of electron inertia the ratio of the parallel wave phase speed of the most unstable mode to the electron thermal speed is $(v_{\rm ph}/v_{Te})_{\gamma\rm max} = (\Omega)_{\gamma\rm max}/(\Omega_A)_{\gamma\rm max}$, where the normalized frequencies $(\Omega)_{\gamma\rm max} \sim 0.44$ and $(\Omega_A)_{\gamma\rm max} \sim 0.71(\tilde{\beta}^{-1})^{1/2}$. For the case of $\tilde{\beta} \ll 1$, where the electron inertial effects dominate, the Landau damping effect is minimized. However, for the marginal plasma pressure $\tilde{\beta} \sim 1$, the waves with comparable magnitudes of wave phase velocity and electron thermal speed are susceptible to the Landau damping.

V. DISCUSSION

We have demonstrated that there are two different types of electromagnetic effects on the high-β blob dynamics: one is the macroscopic field line bending and the other is the modification of microscopic instability. High-β filament with inhomogeneity along the field line (non-uniform curvature and density intensity or sheath boundary condition) makes such bowing of plasma filament and magnetic field lines. The implications of the bending of large pressure plasma is also represented in Ref. 5. As stressed in Ref. 5 the bending motion of such high-β filament can enhance heat exchange between the plasma facing materials and the inner region of SOL forming parallel heat conduction channel.

The coherency of the filament with high temperature depends on the plasma density. According to Sec. IV, the ITER's plasma will be situated in the electromagnetic regime (See Fig. 9) with reduced resistivity and its stability is determined by the drift-Alfvén wave or the electron inertial instability according to the density relation Eq. (16). However, in Sec. IV we neglected the effective gravity force to focus on the electromagnetic effect on the wave instability. This assumption is only valid when the growth rate of instability for blob dissipation

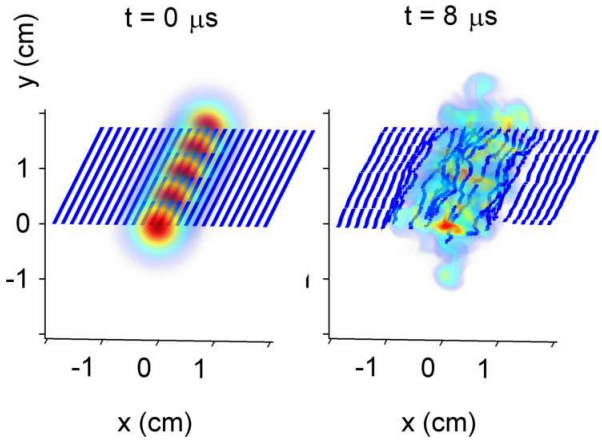

FIG. 12. Stochastic magnetic field lines are calculated during the electron inertial instability with slightly reduced $\tilde{\beta}$. The electron temperature and density are $T_e = 200$ eV and $n_0 = 3 \times 10^{13}$ cm^{-3} respectively.

is larger than a critical time rate of the blob shape deformation due to the macroscopic effective gravitational force, i.e. $\gamma \cdot \tau_m > 1$. The critical blob macroscopic deformation time[16] is $\tau_m \sim (\tilde{n}_b \delta/(n_0 g))^{1/2}$ for the case of no sheath dissipation effects. Then the condition for the negligible macro-dynamics is

$$\frac{\gamma}{\hat{\omega}_*} > \sqrt{\frac{n_0}{\tilde{n}_b}\frac{2\delta}{R}}. \tag{17}$$

Unless the resistive drift wave instability is reduced by large density such as filaments density created by pellet ablation, the condition (Eq. (17)) is usually satisfied for most filamentary structures envisioned for edge plasmas. For the high-β blobs with reduced growth rate, however, the blobs will experience fast macroscopic deformation due to non-uniformities of blob density and effective gravity rather than the microscopic dissipation.

The high-β filaments with reduced growth rate can become more unstable by entering either the electron inertia regime or the electrostatic regime. The blob can move to the electron inertia regime as the blob pressure is declined by macroscopic deformation, and to the electrostatic regime as the temperature is decreased by heat conduction or by other energy loss processes such as inelastic electron collisions with neutrals/impurities in far SOL. As the filament transits to the unstable regimes, cross-field heat conduction will be enhanced by stochastic fields due to the instabilities. See Fig. 12 for an example of such stochastic field lines.

Although our model was able to show some electromagnetic effects on the high-β filamentary structures, there are still some features remained to be added to describe ELM filaments. In particular, large amplitude filament simulation will require nonlinear solver without using the Boussinesq approximation. The fully nonlinear simulation with the large blob/ambient plasma density ratio will produce Alfvén wave slowly propagating inside the filament surrounded by stiff magnetic fields due to dilute background density. Finally, we want to mention that the consideration of increased plasma temperature will require kinetic approach rather than fluid approximation.

VI. CONCLUSION

Electromagnetic blob-filaments properties were studied for high-β plasmas conditions relevant to ITER parameters. Governing equations based on the vorticity, density and parallel component of vector potential equation are considered under assumptions of isothermal electron, cold ion temperature and also Boussinesq approximation with moderate blob-ambient plasma density ratio. Using BOUT++ simulation, we demonstrated the boundary effects on the part of the blob away from the boundary are minimized by the extended Alfvén time scale in high-β filaments. We also showed that high pressure plasma filament can exhibit macroscopic bending along with magnetic field lines because of delayed propagation of polarized potential.

The stability characteristics of plasma filaments with high electron temperature are modified by electromagnetic effects. The linear stability analysis shows that only a small growth rate proportional to resistivity remains for high beta regime. For relatively low beta regime, the electron inertial instability dominate for the high temperature blobs. However, these electromagnetic regime returns to electrostatic regime as plasma temperature decreases.

ACKNOWLEDGMENTS

This material is based upon work supported by the U.S. Department of Energy Office of Science, Office of Fusion Energy Sciences under Award Number DE-FG02-04ER54739 at UCSD. This research used resources of the National Energy Research Scientific Computing Center, a DOE Office of Science User Facility supported by the Office of Science of the U.S. Department of Energy under Contract No. DE-AC02-05CH11231. This research was also supported by the Kwanjeong Educational Foundation.

Prepared by LLNL under Contract DE-AC52-07NA27344.

[1] S. I. Krasheninnikov, D. A. DIppolito, and J. R. Myra, Journal of Plasma Physics **74**, 679 (2008).
[2] D. A. DIppolito, J. R. Myra, and S. J. Zweben, Physics of Plasmas **18**, 060501 (2011).
[3] S. Krasheninnikov, Physics Letters A **283**, 368 (2001).
[4] J. R. Angus, S. I. Krasheninnikov, and M. V. Umansky, Physics of Plasmas **19**, 082312 (2012).
[5] S. Krasheninnikov, D. Ryutov, and G. Yu, J. Plasma Fusion Res. **6**, 139 (2004).
[6] J. R. Myra and D. A. DIppolito, Physics of Plasmas **12**, 092511 (2005).
[7] G. S. Xu, V. Naulin, W. Fundamenski, J. J. Rasmussen, A. H. Nielsen, and B. N. Wan, Physics of Plasmas **17**, 022501 (2010).

[8] P. Manz, D. Carralero, G. Birkenmeier, H. W. Mller, S. H. Mller, G. Fuchert, B. D. Scott, and U. Stroth, Physics of Plasmas **20**, 102307 (2013).
[9] P. Ricci, F. D. Halpern, S. Jolliet, J. Loizu, A. Mosetto, A. Fasoli, I. Furno, and C. Theiler, Plasma Physics and Controlled Fusion **54**, 124047 (2012).
[10] B. I. Cohen, M. V. Umansky, W. M. Nevins, M. A. Makowski, J. A. Boedo, D. L. Rudakov, G. R. McKee, Z. Yan, and R. J. Groebner, Physics of Plasmas **20**, 055906 (2013).
[11] B. Dudson, M. Umansky, X. Xu, P. Snyder, and H. Wilson, Computer Physics Communications **180**, 1467 (2009).
[12] M. Umansky, X. Xu, B. Dudson, L. LoDestro, and J. Myra, Computer Physics Communications **180**, 887 (2009).
[13] J. R. Angus and M. V. Umansky, Physics of Plasmas **21**, 012514 (2014).
[14] X. Q. Xu, R. H. Cohen, T. D. Rognlien, and J. R. Myra, Physics of Plasmas **7**, 1951 (2000).
[15] A. Kukushkin, H. Pacher, V. Kotov, G. Pacher, R. Pitts, and D. Reiter, Nuclear Fusion **53**, 123025 (2013).
[16] J. R. Angus and S. Krasheninnikov, "Inviscid evolution of large amplitude filaments in a uniform gravity field", to be submitted for publication.